

Université Scientifique et Médicale de Grenoble

**INSTITUT DES SCIENCES NUCLÉAIRES  
DE GRENOBLE**

53, avenue des Martyrs - GRENOBLE

ISN 84.02  
January 1984

**ELASTIC AND INELASTIC SCATTERING OF CARBON IONS  
AT INTERMEDIATE ENERGIES**

M. BUENERD, A. LOUIS, J. CHAUVIN, D. LEBRUN, P. MARTIN,  
G. DUHAMEL, J.C. GONDRAND, P. DE SAINTIGNON

*To appear in "Nuclear Physics A"*

Laboratoire associé à l'Institut National de Physique Nucléaire et de  
Physique des Particules.

**ELASTIC AND INELASTIC SCATTERING OF CARBON  
IONS AT INTERMEDIATE ENERGIES**

M. Buenerd, A. Lounis, J. Chauvin, D. Lebrun,  
P. Martin, G. Duhamel, J.C. Gondrand,  
and P. de Saintignon

Institut des Sciences Nucléaires  
53 Avenue des Martyrs  
38026 - Grenoble Cédex (France)

Abstract : Elastic and inelastic scattering has been measured at  $E_{\text{lab}} = 360$  MeV and 1016 MeV for the  $^{12}\text{C} + ^{12}\text{C}$  system, as well as elastic scattering for  $^{13}\text{C} + ^{208}\text{Pb}$  at 390 MeV. Optical model analysis is reported and nuclear surface transparency effects are discussed, together with energy dependence of the nuclear potential. DWBA analysis of data on the  $2^+$ , 4.4 MeV state of  $^{12}\text{C}$  is reported, trends on the energy dependence of mean field excitations are deduced.

#### 1. INTRODUCTION.

The knowledge of the nucleus-nucleus ( $A - A$ ) interaction is an open problem in current heavy-ion physics. The essential of this knowledge is drawn from elastic scattering data. At low incident energy ( $E/A < 20$  MeV), the strong absorption effects dominate the interaction and do not allow a sensitive probing of the nuclear volume. The angular distributions exhibit typical diffraction patterns characteristic of the strong absorption phenomenon. They show no refractive feature sensitive to the real part of the potential and this leads to large ambiguities on the optical potential. For example the system  $^{11}\text{B} + ^{208}\text{Pb}$  at 72 MeV has been found to have a sensitive radius of more than 12 fm, where the real potential value is about 1 MeV<sup>1)</sup>. The probing of the potential is then limited to its very outer tail.

Recently this field has gained a new interest with the occurrence of results casting a new light on the energy dependence of the interaction and providing strong motivations for detailed studies over a broad range of incident energy. A recent work<sup>2,3,4)</sup> has shown the close dependence of the  $A-A$  reaction cross-section  $\sigma_R$  on the nucleon-nucleon ( $N-N$ ) cross-section  $\sigma_{NN}$ . Although the  $N-N$  interaction obviously governs the  $A-A$  interaction, this direct evidence has stimulated both experimental and theoretical investigations. Direct measurements of  $\sigma_R$  have been performed as well as elastic scattering studies,<sup>5,6-10)</sup> addressing to this problem. For the light system  $^{12}\text{C} + ^{12}\text{C}$ , the reaction cross-section data are well reproduced using the eikonal approximation<sup>2,3,11)</sup>. However as can be expected from the simple relationship between the ion-ion potential and  $\sigma_{NN}$ ,<sup>12)</sup> the agreement is not so good for the elastic scattering data<sup>3c,13)</sup>. The picture emerging from this set of data is that of an increasing nuclear surface transparency of

the colliding nuclei with the increasing incident energy per nucleon between about 10 and 85 MeV.

Another open issue concerns the role played by the Pauli-blocking in the A-A interaction. The success of the eikonal approximation to describe the  $\sigma_R$  data for the light systems, seems to rely on the cancellation of the Pauli-blocking and refractive potential contributions. <sup>4,14)</sup> Recently, elaborated calculations of the ion-ion potential based on nuclear matter approach have been performed. <sup>15,16)</sup> They provide potentials critically depending on the incident energy. The repulsive part of these potentials for  $E/A \gtrsim 100$  MeV should manifest itself by characteristic refractive effects in the experimental angular distributions. Although the justification of this approach is rather controversial <sup>17)</sup>, it provides further motivation for measurements over a broad incident energy range.

This paper reports on new elastic and inelastic scattering measurements performed for the systems  $^{12}\text{C} + ^{12}\text{C}$  and  $^{13}\text{C} + ^{208}\text{Pb}$ . The reason for using  $^{13}\text{C}$  projectiles was dictated by considerations related with giant resonance excitations. <sup>18)</sup> Experimental details are given in section II, section III is devoted to the results of the analysis of the  $^{12}\text{C} + ^{12}\text{C}$  system at 1016 MeV and 360 MeV, whereas the results of  $^{13}\text{C} + ^{208}\text{Pb}$  system at 390 MeV are discussed in section IV. A general discussion of the incident energy dependence of the elastic scattering and reaction cross-section is given in section V.

The dominance of the N-N cross-section on the A-A interaction raises the question of the survival of collective effects in A-A collisions at intermediate energy. The inelastic data on the  $2^+$ , 4.4 MeV state of  $^{12}\text{C}$  measured in these experiments may help to answer this question. It will be discussed in section VI.

## II - EXPERIMENTAL PROCEDURE

The data at 30 MeV/n have been measured with the beams provided by SARA, the new heavy ion facility of the ISN Grenoble. This accelerating system consists in two cyclotrons : the old variable energy,  $K = 90$  MeV, cyclotron of the institute has been coupled to a new sector separated booster with  $K_{MAX} = 160$  MeV, providing heavy ion beams at  $(E/A)_{MAX} = 40$  MeV for masses  $A \leq 20$ . This limit has been raised recently to  $A \sim 40$  with the new electron cyclotron resonance (ECR) source now in operation.

The 360 MeV  $^{12}\text{C}$  and 390 MeV  $^{13}\text{C}$  beams were transported to the scattering chamber without momentum analysis. The energy spread of the beams were about  $\frac{\Delta E}{E} \sim 4-5 \cdot 10^{-3}$  at best. The scattered ions were momentum analyzed by means of the magnetic spectrometer. The detection system placed on the focal plane of the spectrometer consisted in a multiwire proportionnal chamber using a delay line system read out for the X and Y planes, an ionization chamber performing energy loss ( $\Delta E$ ) measurement and a stop plastic scintillator coupled to a photomultiplier. The latter provided a fast timing signal used for time of flight and total residual energy measurement. Combination of  $\Delta E$  and TOF signals, properly corrected from their X dependence, provided unambiguous identification of the detected fragments. A spectrum of scattered  $^{12}\text{C}$  in the  $^{12}\text{C} + ^{12}\text{C}$  reaction at 360 MeV is displayed on figure 1. It shows the elastic scattering peak and the excitation of the low-lying levels of  $^{12}\text{C}$ .

The reliability of the physical results reported below depends critically on the accuracy of the angle measurement. This is particularly true for the reaction cross-section. For the  $^{12}\text{C} + ^{12}\text{C}$  system  $\sigma_R$  is essentially determined by the position of the first minimum of the angular distribution and is roughly proportional to the inverse square of this angle. A systematic error of  $0.1^\circ$  on the angle would correspond approximately to 10 percent uncertainty on the reaction cross-section.

In order to reduce the systematic angular uncertainty, a two position (in-beam and out of beam) beam profile monitor (bpm) system has been placed right in front of the entrance collimator of the spectrometer. The position of the central wire of the bpm has been accurately setup to coincide with the geometrical axis of the collimator. By centering the beam both on the target and on the bpm, the offset of the spectrometer could be measured with a precision of  $\pm 0.02$  d°. The inaccuracy of the beam spot centering on the target raises this uncertainty to  $\pm 0.05^\circ$ . During the experiments, this operation was only repeated every few points.

The spot size on the target and the angular divergence of the beam were smaller than  $\approx$  mm and  $0.15$  d° respectively. The angular aperture used for the measurements was  $\Delta\theta = 0.35$  d° except at large angles where  $\Delta\theta = 0.7$  d° was used when the cross-section was found to vary smoothly.

The absolute normalisation was obtained by means of a faraday cup. A double monitoring was performed by using also the response of a plastic scintillator counter set at a fixed angle ( $10$  d°) with respect to the beam direction.

### III - THE $^{12}_C + ^{12}_C$ SYSTEM

This system has been extensively studied over the last few years, at Oak Ridge between 70 and 126 MeV, <sup>19)</sup> at Berkeley between 70 and 290 MeV, <sup>6)</sup> at Berlin at 300 MeV <sup>8)</sup> and at CERN at 1.016 GeV. <sup>7)</sup> Although these latter results have been already partly published, a more complete report on the analysis of these data will be given in this article.

The present data have been analysed using the optical model code HIGENOA allowing the use of up to 500 partial waves. Woods-Saxon shapes have been used to describe the potentials and the coulomb radius parameter has been fixed at  $R_C = 1.3$  fm in the searches.

A - Results at  $E_{\text{Lab.}} = 1016 \text{ MeV}$ .

The angular distribution measured at CERN <sup>7)</sup> is given on figure 2 as the ratio of the experimental cross-section to the Mott cross-section. These data exhibit a typical Fraunhofer diffraction pattern at small scattering angles followed by an exponential fall-off at larger angles ( $\theta > 10^\circ$ ). A similar behaviour has been identified some years ago in  $^4\text{He}$  scattering data as arising from a nuclear rainbow effect. <sup>20)</sup> We shall see below that, in the present data, this particular feature also seems to pin down reasonably well the real potential depth.

The analysis has been carried out using a six parameter potential including volume real and imaginary parts. The searches have been performed for fixed values of the real potential over the range  $15 \text{ MeV} < V_0 < 300 \text{ MeV}$ . For each value of  $V_0$  the other five parameters were varied, using a gridding on  $W_0$  at the earlier stages, until a minimum chi-squared was obtained.

The results are given in table 1. Note the slightly different parameter values reported here and in the previous publication. <sup>7)</sup> This is because the latter were obtained with a too large radial step in the searches ; this does not concern however the analysis reported in the second ref. <sup>7)</sup>. A few interesting remarks can be made concerning these results.

a) The values obtained in table 1 for the reaction cross-section  $\sigma_R$  show a very weak dependence on the set of o.m. parameters, if any ; they are all scattered within  $\pm 30 \text{ mb}$  band around the average value  $\sigma_R = 996 \text{ mb}$ . This value is in fair agreement with that obtained recently in a direct measurement using the attenuation method  $\sigma_R = 960 \pm 25 \text{ mb}$ . <sup>5)</sup> Concerning the present results, one has to keep in mind the uncertainty set on  $\sigma_R$  by the systematic error on the angle measurement <sup>7)</sup>, which leads to  $\sigma_R = 996 \begin{smallmatrix} + 50 \\ -250 \end{smallmatrix} \text{ mb}$ . The agreement with the direct measurement confers a good level of confidence to this value. It will be further discussed in section VI.

b) The chi-squared per point distribution in table 1 exhibits a smooth behaviour with a minimum value centered in the region of real potential depth  $V_0 \sim 120 - 140$  MeV. On each side of this minimum the value of  $\chi^2/N$  increases, rather steeply on the shallow side and more smoothly on the deep side. No minimum on  $\chi^2/N$  is found when the data are limited to  $\theta < 11^\circ$ . Figure 2 compares the experimental results with o.m. calculations corresponding to real well depths of 15, 120 and 200 MeV (see table 1). The large angle data points are much better reproduced with  $V_0 = 120$  MeV than with the other two potentials.

c) The upper figure 3 shows the partial-wave-amplitude  $S_L$  and absorption coefficient  $T_L$  distributions corresponding to the real well depth  $V_0 = 120$  MeV. The amplitudes are seen to have significant values down to  $L \sim 20 - 30$ , corresponding to distances of minimum approach on classical coulomb trajectories of about  $2 - 2.5$  fm, i.e. distances for which the surface nucleons of one nucleus pass through the central region of the partner nucleus.

Let us now consider the semi classical aspects of these results and recall first a few definitions.

The  $T_L$  distribution can be used to define the strong absorption radius  $R_{1/2}$ , quantity which characterizes the system with respect to strong absorption.  $R_{1/2}$  is the distance of closest approach on the coulomb trajectory associated to the partial wave  $L_{1/2}$  for which  $T_L = 1/2$ . For internuclear distances smaller than  $R_{1/2}$ , the absorption dominates, whereas for values larger than  $R_{1/2}$ , partial waves are mostly reflected to the elastic channel. The relationship between  $R_{1/2}$  and  $L_{1/2}$  is given by <sup>21)</sup>,

$$R_{1/2} = \frac{1}{k} \left[ \eta + (\eta^2 + L_{1/2}(L_{1/2} + 1))^{1/2} \right]$$

Where  $\eta$  is the usual Sommerfeld parameter and  $k$  the wave number of the projectile.



Lower figure 3 gives the deflection functions for the coulomb and nuclear potentials as obtained from the classical relations : 21)

$$\theta = 2 \frac{d}{dL} (\text{Re}\phi_L)$$

$\theta$  being the classical deflection angle and  $\phi_L$  the total phase shift

$$\text{Re}\phi_L = \text{Re} \delta_L + \sigma_L$$

Where  $\delta_L$  is the nuclear phase-shift and  $\sigma_L$  the coulomb phase-shift. The nuclear deflection function is obtained from the optical model phase-shifts, whereas the coulomb part is given by

$$\frac{d\sigma_L}{dL} = \text{arc tg } \frac{n}{L}$$

This classical approximation is valid only if one has  $W \ll V$ , condition poorly satisfied in the present case. However, with this restriction in mind, we shall use the above definitions for illustrative purposes and a qualitative discussion.

The total deflection function on fig. 3 has two characteristic extrema : one around  $L = 90$  is the coulomb rainbow which effects are hidden at very small angles ( $\theta \lesssim 1^\circ$ ), and the other around  $L = 40$  corresponds to the nuclear rainbow, associated to the maximum negative deflection angle of classical trajectories. In a classical system it generates a singularity in the cross-section  $\frac{d\sigma}{d\Omega} \frac{bdb}{\sin^2\theta}$  21). The reflexion coefficients in the nuclear rainbow region are not yet very small ( $|\mathcal{R}_L| \sim 0.1$ ), and we have checked that cutting-off the partial waves  $L < 42$  drastically changes the angular distribution in the region  $\theta > 10^\circ$ , whereas a cut-off set at  $L = 20$  is almost ineffective. It has also been verified that progressively

decreasing the depth of the absorbing potential lets the nuclear rainbow show up as a more and more pronounced broad bump in the angular distribution, centered around  $10 - 12^\circ$ . The strong absorption radius associated to  $L_{1/2} = 66$  is  $R_{1/2} = 5.56$  fm. This is noticeably smaller than at low incident energy where it was found to be around 6.8 fm at 70 - 126 MeV.<sup>22)</sup> A plot of the radial dependence of the real part of same potentials of table 1 (see fig. 8) shows that these potentials cross at  $R_S = 4.5$  fm for  $V = 23 \pm 0.5$  MeV,  $R_S$  being the sensitive radius as proposed by G.R. Satchler.<sup>1)</sup> However, it seems that one probes the potential deeper than  $R_S$  in the present case. Indeed, the potentials take very close values ( $V \sim 50$  MeV) down to a radial distance of about  $r \sim 3.6$  fm, if they are deep enough to reach this value. This becomes possible for real potential depths beyond  $V_0 \gtrsim 120$  MeV and provides a straightforward explanation of the chi-squared values of table 1. It seems to confirm that the shallow potentials ( $V_0 \lesssim 80$  MeV) lead to bad chi-squared because of their inability to take large enough values at small distances. In conclusion, it seems that at 1 GeV, one is able to probe the  $^{12}\text{C} - ^{12}\text{C}$  potential at distances as small as  $r \gtrsim 3.6$  fm. To be complete on this point, one must note that the values of the potentials may differ appreciably at larger distances ( $r \gtrsim 5$  fm).

#### B - Results at $E_{\text{lab}} = 360$ MeV.

The measured angular distribution is shown on figure 4. Beyond the diffraction region, the cross-section decreases smoothly up to the maximum angle measured. The optical model analysis gives results which are quite close to those obtained from the analysis of the 1016 MeV data. The chi-squared distribution shows a broad minimum centered in the 150 MeV region of real potential depths (see table 2). This distribution is slightly shifted by about 20 MeV towards deeper potentials with respect to the distribution obtained from the 1016 MeV data.

However, it cannot be stated that the difference is really significant although the real potential is predicted to be rather strongly energy dependent in microscopic models<sup>15,16)</sup> (see also fig. 8). Nevertheless, it is interesting to note that at 300 MeV, the minimum of  $\chi^2/N$  is obtained for an even deeper potential (about 180 MeV).<sup>8)</sup> A systematic study of this trend over a broader incident energy range could provide a test of these models (see discussion below).

The smooth quasi exponential decrease of the differential cross-section observed beyond  $\theta \sim 20^\circ$  can be interpreted in the same terms as at 1016 MeV, with some significant differences however. At 360 MeV, all the potentials adjusted to the data with a real well depth deeper than about 100 MeV reproduce equally well the experimental cross-section beyond  $\theta \sim 20^\circ$ . This is somewhat at variance from what was found at 1016 MeV where only the potentials having a real well depth in the region of the minimum of the  $\chi^2$  distribution could reproduce correctly the exponential fall-off on the differential cross-section. For real well depths  $V_0 \leq 80$  MeV the situation is the same at the two incident energies. As at 1016 MeV, the origin of the  $\chi^2/N$  increase could very well be the inability of the shallow potentials to reach the correct value through the sensitive radial region. The real potentials with  $V_0 \gtrsim 100$  MeV take the same value at  $R \sim 4 - 4.5$  fm which is noticeably larger than at 1016 MeV. At these radial distances the potential is 45 - 30 MeV (fig. 9). The sensitive radius as defined in ref.1 is also found larger at 360 MeV ( $R_s = 5$  fm,  $V = 15.4 \pm 0.7$  MeV).

Figure 5 shows the partial wave amplitudes  $|S_L|$ , transmission coefficients  $T_L$  and deflection function derived from o.m. calculations for the potential  $E$  of table 2. One can see that the partial wave amplitudes in the rainbow region ( $L \sim 30$ ) are in the range  $|S_L| \sim 10^{-2}$ . Nevertheless these amplitudes do contribute to the continuous fall off of the cross-section at large angles. Figure 6 shows the calculated angular distribution for the same potential. The continuous line corresponds

to full calculation. Cutting off partial waves up to  $L = 26$  hardly changes the results whereas a cut-off at  $L = 30$  (including the rainbow minimum, see fig. 5) gives the dotted curve of figure 6, which keeps on oscillating beyond  $\theta \sim 30^\circ$  instead of falling smoothly like the full calculation and the experimental data. We believe that this demonstrates a genuine refraction effect arising from the region of the rainbow minimum. This is rather unexpected in account of the very small amplitude of the partial waves in this region of  $L$ .

IV - THE  $^{13}\text{C} + ^{208}\text{Pb}$  SYSTEM AT  $E_{\text{lab}} = 390$  MeV.

The angular distribution has been measured between  $\theta_{\text{lab}} = 4.1$  and  $18.5^\circ$ . The results are shown on figure 7. It exhibits a characteristic Fresnel diffraction pattern. The radius of the absorbing disc obtained from the quarter point recipe is  $R_{1/4} = 11.95$  fm. The data can be well reproduced with optical model calculations except at the smallest angles where the calculated cross-section is always smaller than the experimental values. The optical model analysis reveals a continuous ambiguity on the real part of the potential over the range of depths investigated (10 - 300 MeV). A sample of o.m. parameter sets is given in table 3. The usual correlation between the depth, radius and diffuseness of the real well is observed. <sup>23)</sup> All these potentials become equal at  $R_s \sim 10.5$  fm where  $V \sim 6.9$  MeV and  $W \sim 2.4$  MeV. Comparing these results to those of ref. 1 for a comparable system, ( $R_s = 12.15$  fm,  $V \sim 1$  MeV) shows that one probes the potential a little further inside in the present case. As observed in the preceding sections for  $^{12}\text{C} + ^{12}\text{C}$ , the potentials deeper than about 80 MeV are identical down to  $R \sim 9.5$  fm, but the  $\chi^2$  values are no more sensitive to this feature.

The imaginary potential also suffers some ambiguity, partly due to a lack of data at small angles. It has been shown some time ago that the imaginary

depth is sensitive to the amplitudes of the  $\sigma/\sigma_{\text{Ruth}}$  oscillations in the region of interference. <sup>1)</sup> This is also true in the present case, although the dependence of the oscillations on  $W_0$  is weak ( $\sigma/\sigma_{\text{Ruth}}^{\text{Max}}$  changes from 1.2 to 1.4 for  $W_0$  changing from 60 to 700 MeV). However equivalent results can be obtained with different combinations of  $W_0$  and geometrical parameters (sets C and E in table 3). Our data are not sufficient in the small angle region to allow a definite conclusion on this point. It will be more carefully investigated in a forthcoming experiment. The imaginary diffuseness is small ( $a' \sim 0.4$  fm). We have verified that fixing  $a'$  at smaller and larger values leads to larger chi-squared values in the searches. This result does not support the recent suggestion that fragile projectiles should have a larger imaginary diffuseness. <sup>24)</sup>

All the potentials providing a good fit to the data also give approximately constant values for the grazing partial wave  $L_{1/2} = 139$  and the associated strong absorption radius  $R_{1/2} \sim 11$  fm (note the good agreement with the quarter point recipe quoted above), and then for the reaction cross-section  $\sigma_R \sim 2900$  mb (see table 3).  $\sigma_R$  and  $R_{1/2}$  obtained here are markedly smaller than those extrapolated from low-energy values (see ref. 22 and second ref. 7) using the geometrical model. Although we are comparing them here with results obtained with a different projectile ( $^{12}\text{C}$ ), we think the comparison is not irrelevant. This indicates the surface transparency is larger than at low incident energy. However the system is still largely governed by strong absorption effects and large ambiguities still affect the potential below  $R \sim 10$  fm.

## V - DISCUSSION OF THE ELASTIC SCATTERING RESULTS

### A - Refraction effects.

These effects are based on the analogy between nuclear scattering and geometrical optics. They widely rely on the concept of trajectory and then they

can be better understood in semi-classical approaches<sup>25)</sup> or in the semi-classical interpretation of quantal calculations.<sup>26,27)</sup> In a recent work (which preprint was received while this paper was being completed), G.R. Satchler and K. McVoy<sup>28)</sup> return to the problematic discussed by R.C. Fuller a few years ago,<sup>26)</sup> concerning the absorptive or refractive origin of the exponential decrease of the elastic cross-section beyond the diffraction region in light systems. The authors criticize the terminology used in the set of recent papers reporting on the observation of a nuclear rainbow effect in the  $^{12}\text{C} + ^{12}\text{C}$  system at several incident energies.<sup>7,9)</sup> They conclude that, in the quoted works, the exponential fall off following the interference pattern (Fraunhofer cross-over) due to the interferences between "nearside" and "farside" amplitudes corresponding to positive and negative deflection angles respectively, is due to the dominance at large angles of the farside amplitudes and then should be referred to as a "farside tail"<sup>26)</sup> rather than a nuclear rainbow effect.

In the results reported here, for the  $^{12}\text{C} + ^{12}\text{C}$  system at 360 MeV and 1016 MeV, we have seen that the data lead to optical model parameters which suffer much less ambiguity than at lower incident energy. Figure 8 shows that the potential in the nuclear surface region ( $R \sim 5 - 10$  fm) is found approximately equal at 360 MeV and 1016 MeV, whereas at  $R = 4$  fm it is markedly stronger at 360 MeV ( $V \sim 48$  MeV) than at 1016 MeV ( $V \sim 36$  MeV). This energy dependence of the potential is in qualitative agreement with the calculations of K.H. Muller.<sup>16)</sup> It is interesting to note that these experimental results are in good agreement with the predictions of the eikonal approximation<sup>13)</sup> (fig. 8). Measurements at higher incident energies (100 - 300 MeV/n), where the data should be more sensitive to the inner potential, should allow a more unambiguous test of calculations ignoring<sup>13)</sup> or taking into account<sup>16)</sup> Pauli blocking effects and they should enlighten the role of the latter in the interaction. We think it is relevant to make another

remark concerning the eikonal approximation potential. The values obtained for this potential are close to those obtained in the folding model analysis of ref. 9. In the latter a renormalisation factor  $N = 0.54$  of the potential fitting the data at  $E_{\text{lab}} = 289$  MeV, was necessary to reproduce the data at 1016 MeV. In the eikonal approximation, the ratio of the potentials calculated for  $E_{\text{lab}} = 360$  MeV and 1016 MeV is 0.59 (see fig. 9), which is almost identical to the value obtained in the folding model (note the difference on the lowest energy). This agreement indicates that the folding model renormalisation factor has its roots in the nucleon-nucleon cross-section as it could be expected.

In order to compare the results obtained here to the situation at lower incident energy, an optical model search has been performed on elastic data measured at 160 MeV at Berkeley<sup>29)</sup>. Equivalent fits could be obtained for real well depths comprised between 20 MeV and 400 MeV with, however, some minima in the  $\chi^2$  distribution around 120, 200, 300 and 400 MeV. This result is in contrast with those reported in section 3 and discussed above. It confirms that one probes more sensitively the inner part of the potential at higher incident energy.

The results on  $^{13}\text{C} + ^{208}\text{Pb}$  are also different from those obtained from  $^{12}\text{C} + ^{12}\text{C}$ . For the latter system, the sensitive radius  $R_S$  as defined in ref. 1) is found noticeably smaller than the strong absorption radius  $R_{1/2}$  (see table 4) the results being sensitive to radii even smaller than  $R_S$ . In contrast, in the  $^{13}\text{C} + ^{208}\text{Pb}$  system,  $R_S$  is close to  $R_{1/2}$  and the analysis is insensitive to the potential at distances smaller than  $R_S$ .

#### B - Energy dependence of the absorption.

Fig. 9 shows the energy dependence of the depth of the imaginary part of the optical potentials deduced from the analysis of  $^{12}\text{C} + ^{12}\text{C}$  elastic data. The low energy points are the Oak-ridge results<sup>19)</sup>, the other points are from the

present analysis of results from Berkeley<sup>29)</sup>, SARA and CERN. The upper three potentials have almost identical geometry, whereas the Oak-Ridge potentials have a larger radius. However, using the radial integrals of the potentials instead of the well depth does not qualitatively affect the picture. We observe that the imaginary depth increases with the increasing incident energy of the projectile up to the 30 MeV/n region where it seems to saturate for the value of  $W_0$  is found approximately equal at 85 MeV/n. Similar conclusions have been reached previously in ref. 9). This cannot be straightforwardly understood in terms of the simplest relationship between the imaginary potential and  $q_{NN}$  (see the discussion in ref. 14). However it is interesting to note that such a behaviour has been predicted qualitatively by H. Orland and R. Schaeffer in terms of the competition between one-body and two-body viscosity effects in the energy dissipation process.<sup>33)</sup> However one must take this agreement with some care for the imaginary potentials are not completely unambiguous.<sup>8)</sup>

Upper fig. 10 shows the distribution of the transmission coefficients  $T_L$  as a function of the internuclear distance of minimum approach  $D$  associated to the partial wave angular momentum  $L$  assuming a coulomb trajectory. This assumption being not rigorous, fig. 10 must be considered as a qualitative picture of the absorption in the reaction considered. It provides an nice illustration of the global evolution of the absorption with the incident energy of the projectile. Lower fig. 10 shows the overlap of the density distribution of the two nuclei along a radius at the strong absorption distance as defined in section 3 deduced from upper fig. 10 for the three incident energies. The decrease of  $R_{1/2}$  with the increasing incident energy unmasks the real potential over a wider part of the nuclear periphery and allows refraction effects to appear in the elastic cross-section.

This evolution of the absorption is not unexpected if one considers the  $A - A$  interaction in terms of its relationship with the elementary  $N - N$  interaction. The  $N - N$  interaction is a basic ingredient of the  $A - A$  potential. It appears as such in e.g. the eikonal approximation<sup>13,30,34)</sup> or the folding model<sup>22)</sup>



or the nuclear matter <sup>16)</sup> approach of the problem. The eikonal approximation directly relates the attenuation length of the projectile to the average  $N - N$  cross-section  $\sigma_{NN}$ . The latter decreases by an order of magnitude between 10 and 100 MeV incident energy. <sup>31)</sup> The conventional nucleon mean free path which is inversely proportional to  $\sigma_{NN}$  (i.e.,  $\lambda \sim (\rho\sigma_{NN})^{-1}$ ), should then increase over this range and the nuclear surface transparency is expected to increase correspondingly (see the discussion given in ref. 14). The overlap of the two densities at 2.4 GeV lab. shown on lower figure 10 corresponds to a calculation in the eikonal approximation. It suggests that at this energy the absorption area is still shrinking. Then refraction effects should appear even more prominently in the elastic cross-section at higher energies. Experimental measurements of the elastic cross-section over the incident energy range extending up to the minimum of the nucleon - nucleon cross-section ( $E/A \sim 300$  MeV) have been planned in order to explore the energy dependence of the  $A - A$  potential.

It has been shown in a separate publication that eikonal calculations of the elastic cross-section can account reasonably well for the data. <sup>13)</sup> For  $^{12}\text{C} + ^{12}\text{C}$  the better agreement of these calculations with the data at lower incident energies is likely due to the more peripheral character of the reaction at the low incident energies for which the higher order (rescattering) terms of the Glauber development are then negligible. <sup>12,34)</sup> This is no more true at higher incident energies where the deeper interpenetration of the two nuclei makes it likely that rescattering terms should contribute to the transition amplitude. Their neglect leads to a poorer agreement of the eikonal approximation calculations with the data at large angles where rescattering terms can contribute appreciably. <sup>13)</sup> However for this system the absorption seems to be reasonably well described by the model and the calculated value of  $\sigma_R$  is in good agreement with the data at the two incident energies (see fig. 11). <sup>13)</sup> The situation is found different for the  $\text{C} + ^{208}\text{Pb}$  systems. Correcting the straight line trajectory assumption of the

eikonal approximation for coulomb deflection leads to theoretical predictions which markedly overestimate the experimental values at 30 MeV/n ( $\sigma_R^{\text{exp}} = 2900$  mb,  $\sigma_R^{\text{th}} = 3440$  mb) and 85 MeV/n ( $\sigma_R^{\text{exp}} = 2500$  mb,  $\sigma_R^{\text{th}} = 3370$  mb). Further work is required to understand this discrepancy.

The phenomenon of increasing nuclear surface transparency can be also illustrated with the evolution of the reaction cross-section with the incident energy. Figure 11 shows the experimental values obtained in the present work along with those obtained in other experiments, (2,5,6,8,19) compared with the calculations of ref. 2. The data from ref. 8 have been reanalyzed and the same value of  $\sigma_R = 1400$  mb has been obtained with different imaginary well depths. On figure 11,  $\sigma_R$  follows the same trend as the N - N cross-section, decreasing from around the coulomb barrier down to a minimum in the region of minimum  $\sigma_{\text{NN}}$  and rising again slowly beyond this value.

Similar trends are observed for the  $^{208}\text{Pb}$  target. Figure 12 shows the energy dependence of the reduced strong absorption radius  $R_{1/2}$  for  $^{16}\text{O}$  and  $^{12,13}\text{C}$  projectiles on  $^{208}\text{Pb}$  which decreases noticeably over the energy range for which data are available. The  $\sigma_R$  dependence on the incident energy  $E$  shows similar trends as observed for  $^{12}\text{C} + ^{12}\text{C}$  (see second ref.7).

#### VI - INELASTIC SCATTERING TO THE $(J^{\pi}, E_x) = (2^+, 4.4 \text{ MeV})$ STATE.

We have seen in the previous sections that the incident energy dependence of the elastic scattering observable seems to support the assumption that the interaction mechanism is dominated by N - N collisions when the incident energy increases. If one now turns to the absorbed flux in these collisions, theoretical considerations lead to a general picture where at low energy (say around 10 MeV/n) the Pauli-blocking effects are strong and the mean field effects (one-body viscosity) are responsible for the essential of the inelasticity in heavy ion collisions, whereas at high energy (beyond 100 MeV/n) most of the inelasticity is

accounted for by incoherent N - N collisions (two body viscosity).<sup>33,35)</sup> An interesting question is about the information on this point which can be obtained from experiments. One such possibility is offered by the excitation of collective transitions which take place via mean field interactions and are well described by collective models. We present below some results on the incident energy dependence of the ( $2^+$ , 4.4 MeV) state measured in the  $^{12}\text{C} + ^{12}\text{C}$  experiments.

Inelastic scattering data to the first excited  $J^\pi = 2^+$ ,  $E_x = 4.4$  Mev state of  $^{12}\text{C}$  have been taken at the two incident energies of 1016 MeV and 360 MeV. The results are shown on fig. 13 compared to DWBA calculations using the standard collective model form factor and a deformation parameter  $\beta = 0.6$ . The calculated cross-sections show little dependence (less than about 10%) on the optical model parameters used in the region of the minimum  $\chi^2$  (say 60 MeV  $\leq V_0 \leq$  200 MeV) for the two incident energies. In both cases the fits obtained are rather satisfactory although the amplitudes of the oscillations of the angular distribution are not very well reproduced by the calculations. However this has a negligible effect on the integrated cross-sections which we want to estimate and which depend only on gross features of the angular distribution.

We have also evaluated in the same way the integrated cross-sections at lower incident energies using the data from refs. 8, 19 and 29.

The results are shown on figure 14. Over the range 5 - 85 MeV/n, the cross-section for the excitation of the  $2^+$  state decreases by a quite appreciable fraction (upper on the figure). We think this reflects the energy dependence of the A-A interaction on the N-N interaction as it can be seen in the folding model<sup>22)</sup> approach of the transition. In this model the DWBA form factor  $\Delta V$  is described by the folding integral :

$$\Delta V (R) = \int \rho_D(\mathbf{r}) \delta\rho_T(\mathbf{r}') v(\vec{R} + \vec{r} - \vec{r}') d\vec{r} d\vec{r}'$$

where  $\rho_D$  and  $\delta\rho_T$  are the projectile density and the target transition density describing

the excitation, respectively.  $v$  is an effective interaction different of the nucleon-nucleon interaction describing the free scattering but related to it and expected to show a similar energy dependence. Then the transition potential may decrease along the nucleon-nucleon cross-section because of this relationship. It can be noted that in all the cases investigated here, no adiabatic inhibition of the transition is expected. <sup>18,36)</sup> The significant quantity for the point we want to investigate, i.e. the competition between the contribution of coherent and incoherent processes to the total inelasticity, is the fraction of the reaction cross-section  $\sigma_R$  taken away by the cross-section  $\sigma_{2+}$  for the excitation of the  $2^+$ , 4.4 Mev state. Lower fig. 13 shows the energy dependence of this ratio  $\sigma_{2+}/\sigma_R$  which decreases by a factor of about 3 over the covered range of incident energy, confirming that mean field effects are decreasing over this range. This is to our knowledge the first direct experimental information on this problem. However in the present stage we do not know of any theoretical prediction, which could be confronted to this result.

## VII - SUMMARY

Elastic scattering data from the  $^{12}\text{C} + ^{12}\text{C}$  and  $^{13}\text{C} + ^{208}\text{Pb}$  reactions in the intermediate energy domain have been analyzed in the frame work of the optical model. The results of the analysis at 30 MeV/n show that in this energy range the nuclear surface is more transparent than at low energies, the nuclear surface transparency is even larger at 85 MeV/n. This effect can be traced back in the energy dependence of the nucleon-nucleon cross-sections. The eikonal potential obtained from the latter provides a clear interpretation of the folding model analysis results obtained in other works.

The inelastic scattering cross-section to the  $2^+$ , 4.4 MeV state in the  $^{12}\text{C} + ^{12}\text{C}$  reactions has been shown to decrease with the increasing incident energy likely for the same reason that the surface transparency increase i.e. the energy dependence of the nucleon-nucleon cross-section. More interesting is the ratio  $\sigma_{2^+} / \sigma_T$  which also decreases with E indicating a lower contribution of the mean-field effects to the inelasticity at higher E. The above quoted points will be subjects of further experimental investigations.

#### VIII - ACKNOWLEDGEMENTS

The authors are indebted to G.R. Satchler for pointing out the anomaly in the optical model analysis of first ref. 7. They also acknowledge the participation of M.E. Brandan and A. Menchaca-Rocha to some of the measurements reported here.

REFERENCES

- (1) G.R. Satchler, in Reactions between complex nuclei, NHPC, 1974.
- (2) R.M. DeVries and J.C. Peng, Phys. Rev. C 22 (1980) 1055.
- (3) J.C. Peng, R.M. DeVries and N.J. Digiaco, Phys. Lett. 97B (1981) 244.
- (4) N.J. Digiaco, R.M. DeVries and J.C. Peng, Phys. Rev. Lett, 45 (1980) 527.
- (5) C. Perrin et al., Phys. Rev. Lett. 49 (1982) 1905 ; R. DeVries et al.  
Phys. Rev. C26 (1982) 301.
- (6) A.J. Cole et al., Phys. Rev. Lett. 47 (1981) 1705.
- (7) M. Buenerd et al., Phys. Rev. C 26 (1982) 1299, and Phys. Lett. 102B (1981) 242.
- (8) H.G. Bohlen et al., Z. Phys. A308 (1982) 121.
- (9) M.E. Brandan, Phys. Rev. Lett. 49 (1982) 1132.
- (10) S. Kubono et al., Phys. Lett. 127B (1983) 19.
- (11) P.J. Karol, Phys. Rev. C11 (1975) 1203.
- (12) R.J. Glauber, Lectures on theoretical physics, Interscience,  
New-York, 1959, vol. 1.
- (13) J. Chauvin, D. Lebrun, A. Lounis, and M. Buenerd, Phys. Rev. C28 (1983) 1970.
- (14) D.M. Brink and G.R. Satchler, J. Phys. G 7 (1981) 43.
- (15) see e.g. R. Sartor, A. Faessler, S.B. Khadkikar and S. Krewald  
Nucl. Phys. A359 (1981) 467 and refs. therein.
- (16) K.H. Muller, Z. Phys. A295 (1980) 79.
- (17) G.R. Satchler, Nucl. Phys. A409 (1983) 3.
- (18) M. Buenerd, in Nuclear Physics with heavy ions, P. Braun-Munzinger  
Harwood edit. (1984), to be published.
- (19) R.M. Wiedland, R.G. Stockstad, G.R. Satchler, and L.D. Rickertsen,  
Phys. Rev. Lett. 37 (1976) 1458 ; R.G. Stockstad et al., Phys. Rev. C20  
(1979) 655.

- (20) D. A. Goldberg, S.M. Smith, and G.F. Burdzik, Phys. Rev. C10 (1974) 1362.
- (21) W.E. Frahn, Heavy-ion high spin states and nuclear structure, IAEA, Vienna 1975, vol.1.
- (22) G.R. Satchler and W.G. Love, Phys. Rev. 55 (1979) 183.
- (23) P.E. Hodgson, Nuclear heavy ion reactions, Clarendon press, Oxford, 1978.
- (24) G.R. Satchler et al., Phys. Lett. 128B (1983) 147.
- (25) R. Schaeffer, Nuclear Physics with Heavy Ions and Mesons, R. Balian, M. Rho, G. Ripka edit., NHPC 1978, and references therein.
- (26) R.C. Fuller, Phys. Rev. C 12 (1975) 1561.
- (27) R. Da Silveira, Phys. Lett. 45B (1973) 211 ; N. Rowley and C. Marty, Nucl. Phys. A266 (1976) 494.
- (28) G.R. Satchler and K. McVoy, ORNL prepint.
- (29) M.E. Brandan, private communication.
- (30) W. Czyz and L.C. Maximon, Ann. Phys. 52 (1969) 59.
- (31) W.N. Hess, Rev. Mod. Phys. 30 (1958) 368.
- (32) C. Glmer et al., Phys. Rev. C. 18 (1978) 205
- (33) H. Orland, Proc. of XVII<sup>th</sup> Nucl. Meeting on Nucl. Phys., Bormio (Italy) January 22 - 27, 1979.
- (34) V. Franco and G.K. Varma, Phys. Rev. C 18 (1978) 349.
- (35) see e.g. B. Sinah, Phys. Lett. 99B (1981) 89, and references therein.
- (36) K. Broglia, C.H. Dasso and Aa. Winther, Phys. Lett. 61B (1976) 113.
- (37) J. Jaros et al. Phys. Rev. C 18 (1978) 2273.

Table caption

Table 1 :

Optical model parameters obtained from the analysis of  $^{12}\text{C} + ^{12}\text{C}$  elastic scattering data at 1016 MeV, for fixed values of the real well depth. The last two columns give the calculated reaction cross-section and the minimum chi-squared per point value obtained in the search.

Table 2 :

Same as table 1 for  $^{12}\text{C} + ^{12}\text{C}$  at 360 MeV

Table 3 :

Same as table 1 for  $^{13}\text{C} + ^{208}\text{Pb}$  at 390 MeV.

Table 4 :

Strong absorption radius  $r_{1/2}$ , sensitive radius  $r_g$  (see ref. 1 and text) and smaller radius for which the data show some sensitivity to the real potential, for the three studied systems, given in reduced values.



Table 1

	V	r	a	W	r'	a'	$\sigma_R$	$\chi^2/N$
A	15	1.29	0.57	37.80	1.03	0.46	966	12.
B	40	1.03	0.67	34.20	1.00	0.55	971	9.3
C	60	0.91	0.71	39.13	0.95	0.63	995	7.3
D	80	0.83	0.75	40.57	0.917	0.72	1027	5.1
E	100	0.77	0.84	47.35	0.95	0.59	1005	3.6
F	120	0.71	0.84	34.02	0.96	0.619	1040	2.3
G	140	0.6	0.90	45.10	0.96	0.58	1001	2.3
H	200	0.55	0.98	43.11	0.99	0.53	994	3.7
I	300	0.41	1.06	47.68	0.98	0.53	1007	4.8

Table 2

	V	r	a	W	r'	a'	$\sigma_R$	$\chi^2/N$
	(MeV)	(fm)	(fm)	(MeV)	(fm)	(fm)	(nb)	
A	46	1.01	0.52	37.0	0.86	1.02	1500.	13
B	60	0.94	0.62	55.3	0.84	0.78	1259	11
C	80	0.87	0.65	57.4	0.85	0.75	1247	8.5
D	100	0.84	0.67	49.2	0.92	0.72	1258	7.1
E	120	0.79	0.70	47.5	0.92	0.72	1258.	9
F	150	0.74	0.72	55.	0.88	0.72	1257	4.9
G	180	0.69	0.79	56.7	0.89	0.73	1268.	4.8
H	220	0.68	0.74	49.	0.95	0.67	1242	7.8
I	300	0.62	0.76	62.5	0.91	0.69	1264	7.1

Table 3

	V	r	a	W	r'	a'	$\sigma_R$	$\chi^2/N$
A	20	1.20	0.73	48.6	1.11	0.43	2890	1.
B	40	1.12	0.80	65.7	1.12	0.38	2895	1.
C	80	1.02	0.87	74.6	1.11	0.38	2883	1.1
D	200	0.91	0.90	76.2	1.11	0.38	2890	1.1
E	80	0.92	1.07	700	0.81	0.65	2930	0.95

Table 4

System	$E_{\text{Lab}}$	$r <$	$r_s$	$r_{1/2}^{\text{exp}}$
$^{12}\text{C} + ^{12}\text{C}$	1016	0.92	1.09	1.35
$^{12}\text{C} + ^{12}\text{C}$	360	0.79	0.98	1.21
$^{13}\text{C} + ^{208}\text{Pb}$	390	1.27	1.27	1.32

Figure Captions

Figure 1 :

Momentum spectrum of  $^{12}\text{C}$  measured in  $^{12}\text{C} + ^{12}\text{C}$  at  $E_{\text{lab}} = 360$  MeV.

Figure 2 :

Elastic scattering angular distribution measured in  $^{12}\text{C} + ^{12}\text{C}$  at  $E_{\text{lab}} = 1016$  MeV. The curves are optical model fits with fixed real well depths of 15 MeV (dashed), 120 MeV (solid), and 200 MeV (dotted).

Figure 3 :

Upper : partial wave amplitudes  $|S_L|$  and absorption coefficients  $T_L$  distributions for potential E of table 1, as functions of the angular momentum L.  
Lower : coulomb, nuclear, and coulomb + nuclear deflection functions obtained from classical relations as described in the text. The upper and lower horizontal scales are the same.

Figure 4

Elastic scattering angular distribution of  $^{12}\text{C} + ^{12}\text{C}$  at  $E_{\text{lab}} = 360$  MeV compared with best optical model fit (parameter set E in table 2)

Figure 5

Same as figure 3 for  $^{12}\text{C} + ^{12}\text{C}$  at 360 MeV. Only the coulomb + nuclear deflection function is shown.

Figure 6

Calculated elastic scattering angular distributions for the best fit

potential (set E in table 2), including all partial waves (solid line) and with a cut-off on partial waves below the rainbow angle (dotted line).

Figure 7 :

Experimental elastic scattering angular distribution fitted with optical model calculations (set C in table 3)

Figure 8 :

Woods-Saxon potentials obtained from the analysis (see tables 1, 2) for  $^{12}\text{C} + ^{12}\text{C}$  at 1016 MeV (left) and at 360 MeV (right) compared to the eikonal approximation prediction (dotted lines).

Figure 9 :

Energy dependence of the imaginary potential for the  $^{12}\text{C} + ^{12}\text{C}$  system. The low energy points are from ref. 19. The other points are from the present analysis. The curve is an eye-guide.

Figure 10 :

Upper : Transmission coefficient  $T_L$ , as a function of the distance of minimum approach assuming coulomb trajectories, for the laboratory incident energies of 161 MeV (dash-dotted line, data from refs. 6, 29), 360 MeV (dashed line) and 1016 MeV (full line). Lower : overlap of  $^{12}\text{C}$  densities at the strong absorption distance deduced from above (see text) for 161 MeV, 360 MeV and 1016 MeV. The picture at 70 MeV is from ref. 22 (mixed double dotted line). The  $T_L$  values and density overlap (dotted lines) at 2400 MeV are obtained from a calculation of the transparency function in the eikonal approximation (see ref. 13).

Figure 11 :

Reaction cross-section for the  $^{12}\text{C} + ^{12}\text{C}$  system as a function of the laboratory incident energy per nucleon. The data points are from refs. 19 (open circles), 6 (full squares), 8 (half-full square), 5 (half-full circles), 37 (triangles), and from the present work and ref. 7 (open squares). The curve is a calculation in the eikonal approximation from ref. 2.

Figure 12

Reduced strong absorption radius  $r_{1/2}$  defined as  $R_{1/2} = r_{1/2} (A_p^{1/3} + A_t^{1/3})$ , as a function of the laboratory incident per nucleon for  $^{12,13}\text{C} + ^{208}\text{Pb}$  (full circles, ref. 22 ; full square, second ref. 7 ; open squares present work) and  $^{16}\text{O} + ^{208}\text{Pb}$  (open circles, ref. 32). The curve is an eye-guide.

Figure 13 :

Angular distributions for  $^{12}\text{C}$  inelastic scattering to the 4.4 MeV,  $2^+$  state of  $^{12}\text{C}$  at 1016 MeV (left) and 360 MeV (right), compared to standard collective model DWBA calculations.

Figure 14 :

Upper : energy dependence of the integrated cross-section for the 4.4 MeV,  $2^+$  state of  $^{12}\text{C}$ . Lower : the same for the ratio of the  $2^+$  cross-section to the reaction cross-section. The curves are to guide the eye.

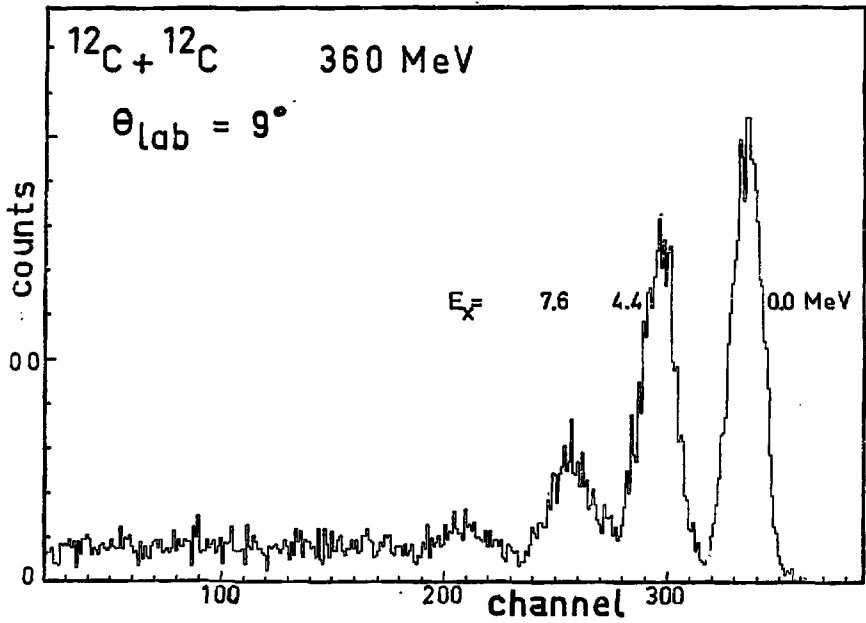


fig 1



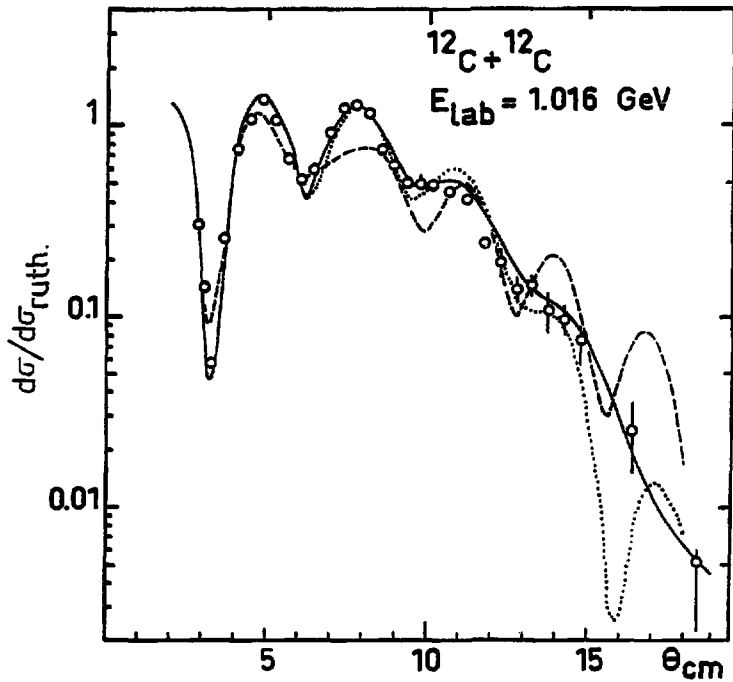
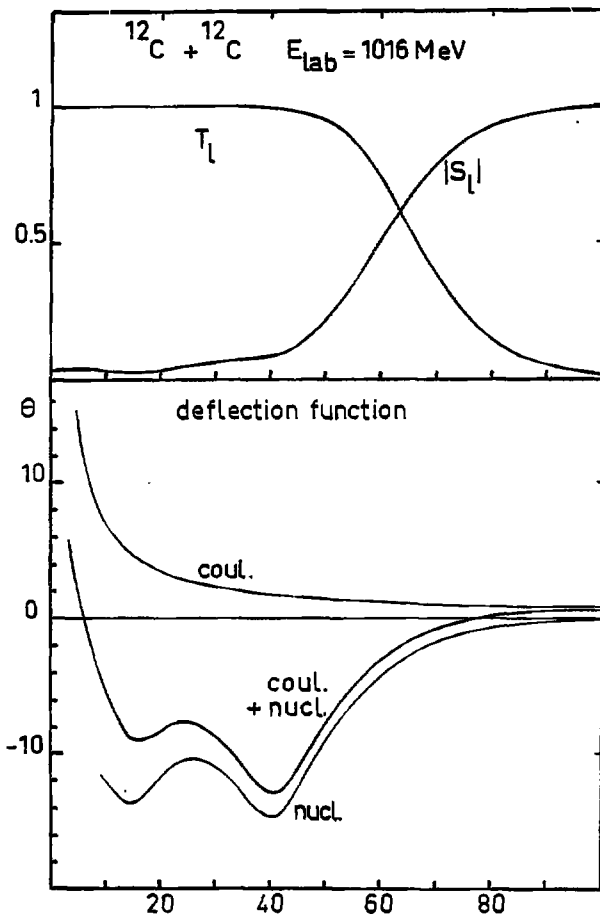


Fig 2



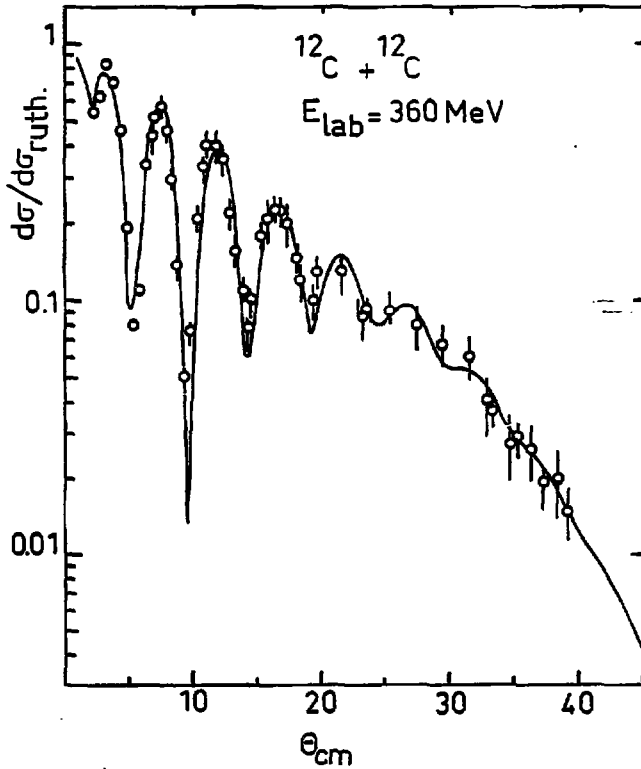
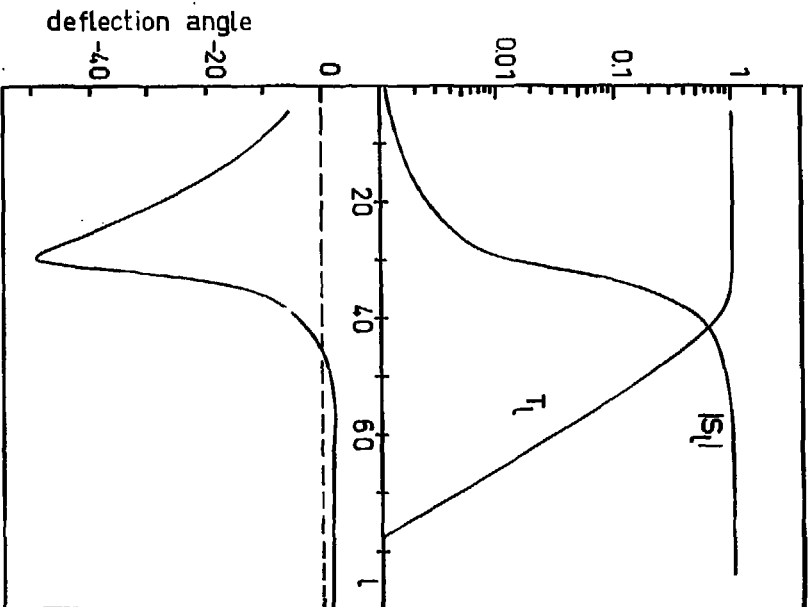
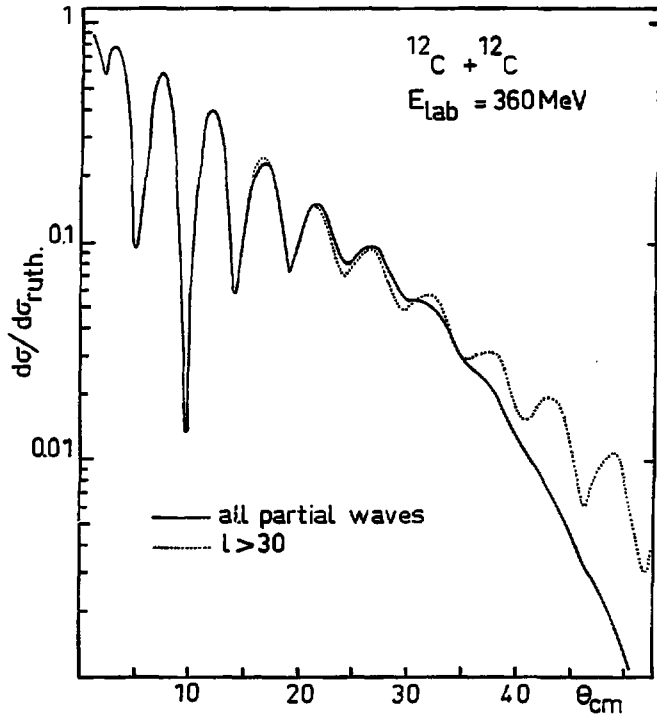
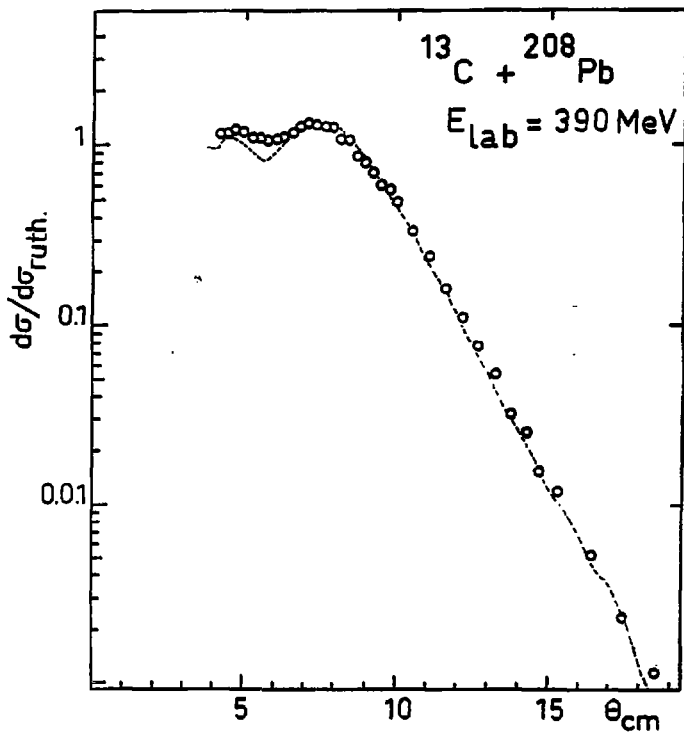


Fig 4







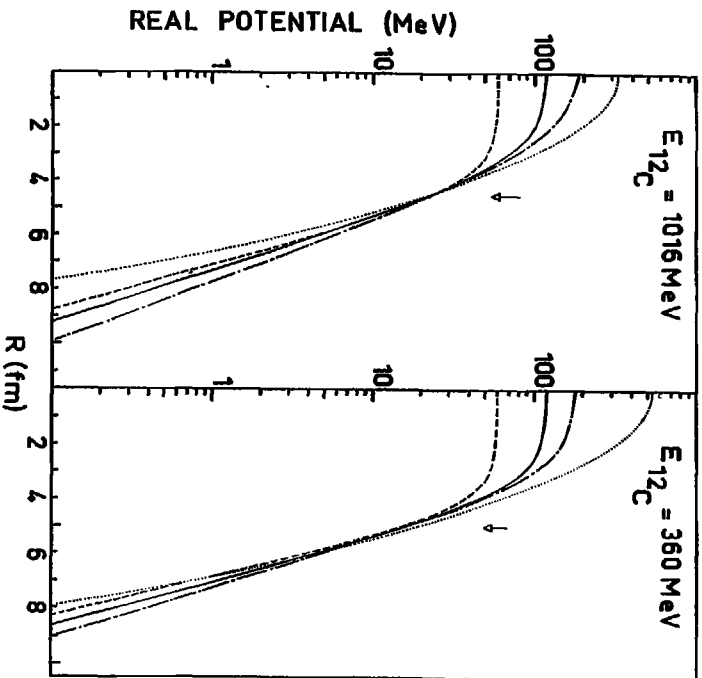
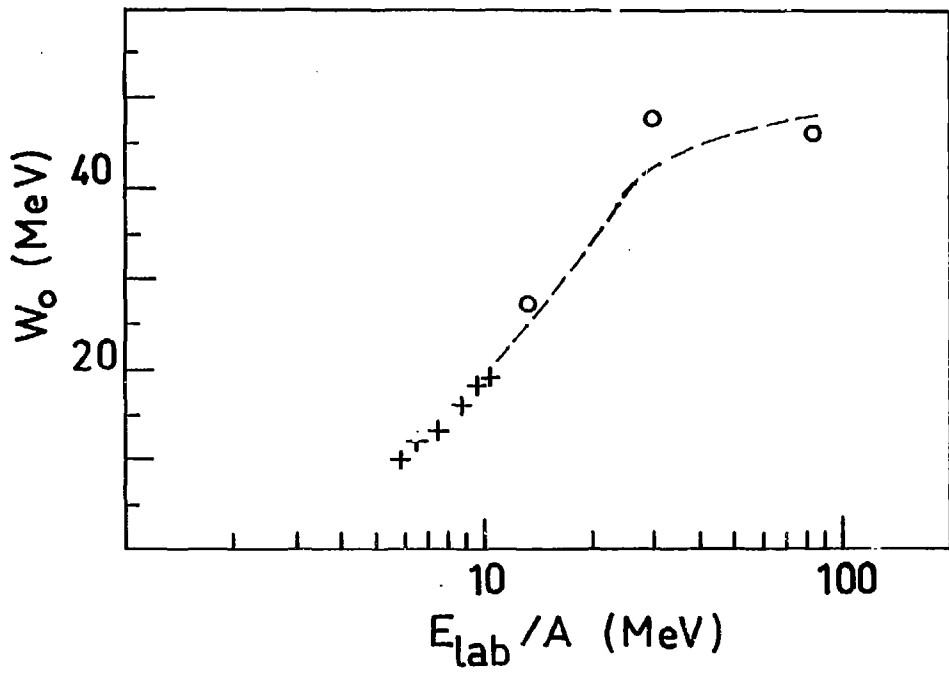


Fig 8





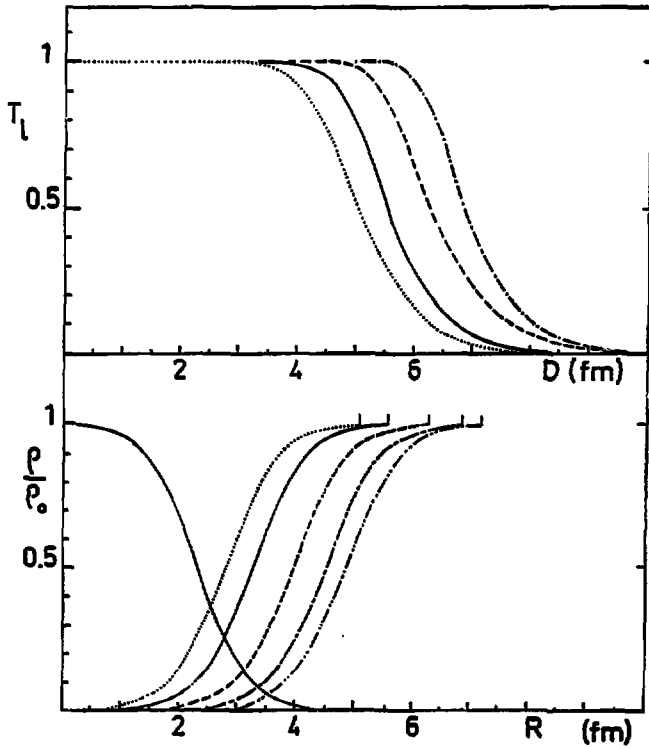
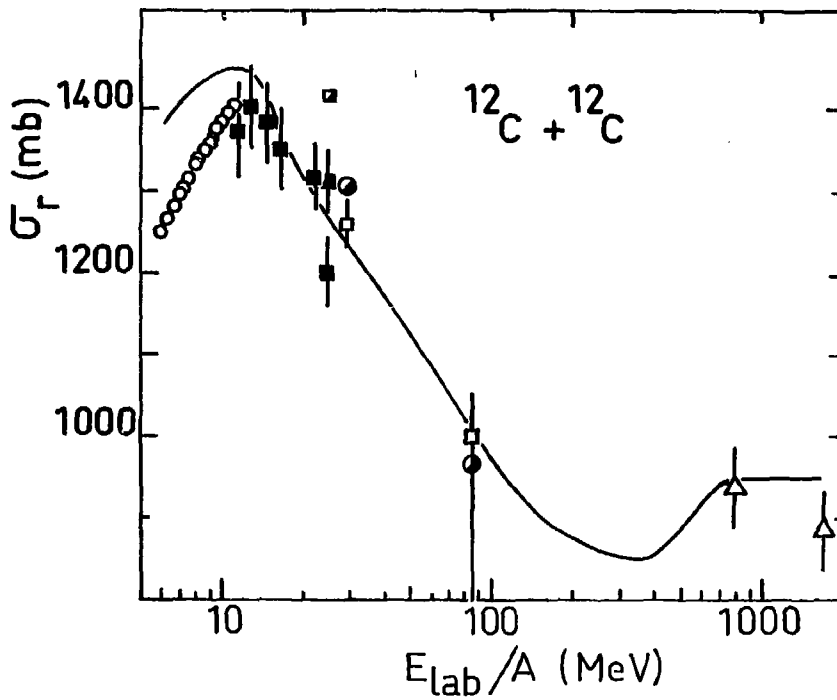
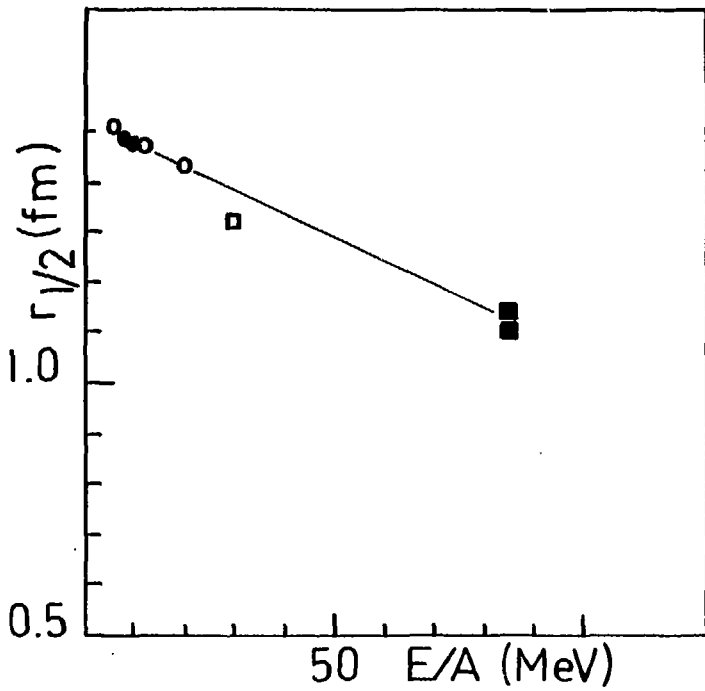
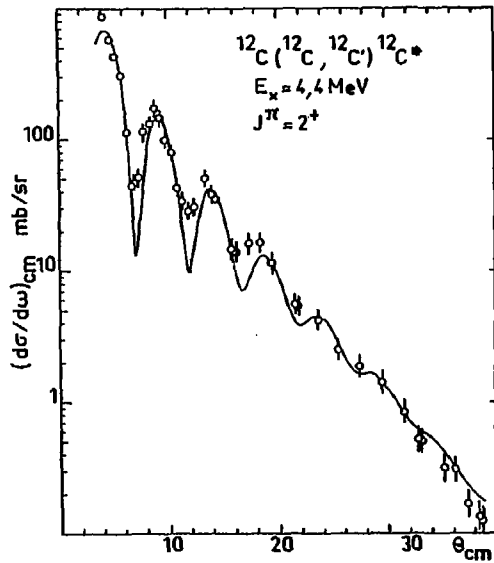
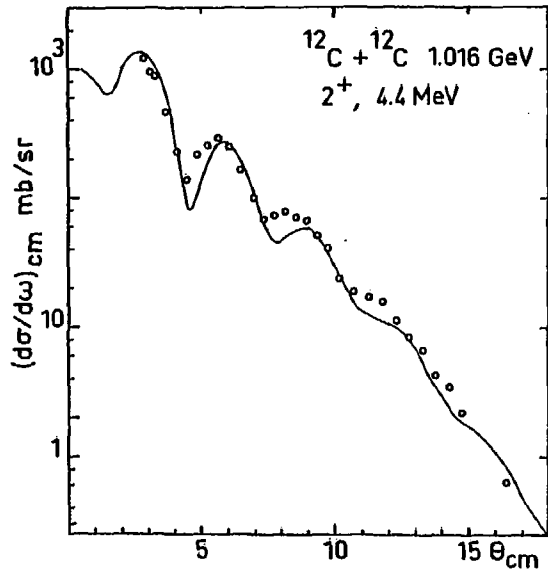


fig 10







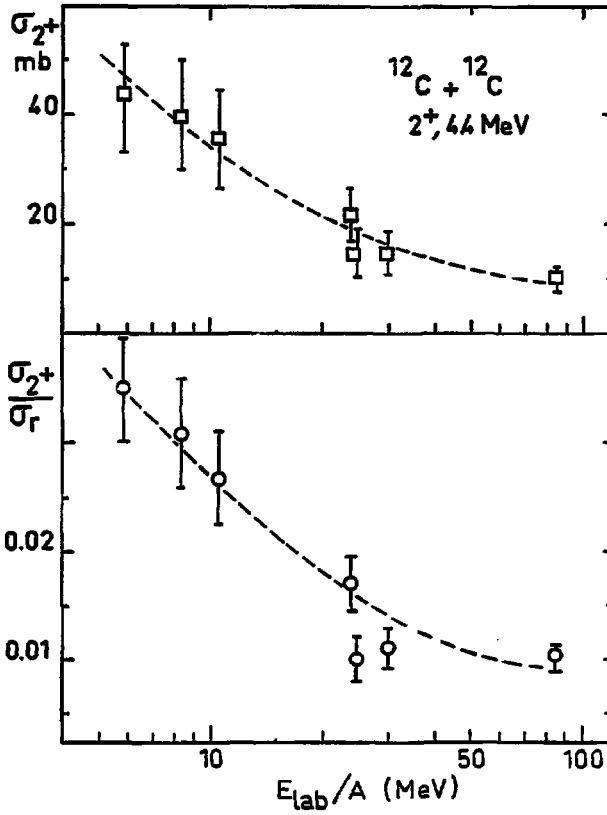


Fig 14